RESEARCH PAPER

Study of subsonic–supersonic gas flow through micro/nanoscale nozzles using unstructured DSMC solver

Masoud Darbandi · Ehsan Roohi

Abstract We use an extended direct simulation Monte Carlo (DSMC) method, applicable to unstructured meshes, to numerically simulate a wide range of rarefaction regimes from subsonic to supersonic flows through micro/nanoscale converging–diverging nozzles. Our unstructured DSMC method considers a uniform distribution of particles, employs proper subcell geometry, and follows an appropriate particle tracking algorithm. Using the unstructured DSMC, we study the effects of back pressure, gas/surface interactions (diffuse/specular reflections), and Knudsen number on the flow field in micro/nanoscale nozzles. If we apply the back pressure at the nozzle outlet, a boundary layer separation occurs before the outlet and a region with reverse flow appears inside the boundary layer. Meanwhile, the core region of inviscid flow experiences multiple shock-expansion waves. In order to accurately simulate the outflow, we extend a buffer zone at the nozzle outlet. We show that a high viscous force creation in the wall boundary layer prevents any supersonic flow formation in the divergent part of the nozzle if the Knudsen number exceeds a moderate magnitude. We also show that the wall boundary layer prevents forming any normal shock in the divergent part. In reality, Mach cores would appear at the nozzle center followed by bow shocks and expansion region. We compare the current DSMC results with the solution of the Navier–Stokes equations subject to the velocity slip and temperature jump boundary conditions. We use OpenFOAM as a compressible flow solver to treat the Navier–Stokes equations.

1 Introduction

Attention to Micro/Nano-Electro-Mechanical Systems (MEMS-NEMS) has grown enormously in leading technologies such as micro/nano-technologies since a few years ago. This has led to the development of an increasing number of extremely small devices. As the hydrodynamic diameter of a conduit decreases to scales comparable with the mean free path of the flow particles moving through it, the continuum flow assumptions behind extracting the Navier–Stokes (NS) equations deteriorate rapidly. In other words, the gas can no longer be in thermodynamic equilibrium and a variety of rarefaction effects can take place. The weight of rarefaction can be measured by defining the flow Knudsen number, which is the ratio of gas mean free path (λ) to the conduit height, $Kn = \lambda/H$ in a 2D channel flow. Different non-equilibrium regimes including slip ($0.001 < Kn < 0.1$), transition ($0.1 < Kn < 10$), and free molecular ($Kn > 10$) ones have already been categorized in micro/nanoscale geometries.

One of the basic geometries utilized in MEMS and NEMS is the converging–diverging nozzle. Performing a varying cross section, the flow in micro/nanoscale nozzle may experience different rarefaction regimes simultaneously. For example, it may experience both continuum and slip flow regimes at the convergent part while the divergent part may experience transition and free molecular regimes. Evidently, the NS equations; subject to the velocity slip and temperature jump boundary conditions,

M. Darbandi (✉) · E. Roohi
Center of Excellence in Aerospace Systems, Department
of Aerospace Engineering, Sharif University of Technology,
P.O. Box 11365-8639, Tehran, Iran
e-mail: darbandi@sharif.edu

may be proposed to solve the micro/nanoscale nozzle flows. However, the encountered obstacles promote the researchers to choose the kinetic-based approaches, such as the direct simulation Monte Carlo (DSMC) (Bird 1994), to simulate flow in such small scales with a wide range of rarefaction regimes. Literature shows that DSMC has been largely used to predict the flow field inside micro/nanoscale devices such as micro/nanoscale channels (Xue et al. 2003; Wang and Li 2004; Roohi et al. 2009; Roohi and Darbandi 2009; Yang et al. 2009) and nozzles (Alexeenko et al. 2002, 2006; Louisos and Hitt 2005; Liu et al. 2006; Xie 2007). We mainly focus on the activities performed in the latter ones.

Alexeenko et al. (2002) simulated flow through axisymmetric and 3D micronozzles using both DSMC and NS solvers. They observed that the viscous effects would dominate the gas expansion and reduce the thrust mainly due to significant wall shear stress appearances. They investigated the effect of tangential momentum accommodation coefficient on the flow behavior and showed that the flow would depend on this coefficient weakly if it increases from 0.8 to 1. Louisos and Hitt (2005) solved the NS equations and studied the effects of micronozzle geometry on its performance. They reported a remarkable reduction in the nozzle thrust as the divergent angle exceeded over 60°. They reported that the subsonic boundary layer would restrict the flow and reduce the effective exit area. In another attempt, Alexeenko et al. (2006) used a coupled thermal-fluid analysis (finite-element DSMC) to study the performance of high temperature gas flow through MEMS-based nozzles. They calculated the temporal flow field variation and the nozzle temperature. In addition, they reported the operational time limit for thermally insulated and convectively cooled nozzles. Liu et al. (2006) simulated flow through small-scale nozzles using the DSMC and the NS equations with slip and jump boundary conditions. They studied the effects of inlet pressures, Reynolds number, and micronozzle geometry and reported that the continuum-based solutions would show obvious deviations from the DSMC results as Kn number exceeds 0.045. Xie (2007) simulated low Knudsen number micronozzle flows using DSMC and solving the NS equations. He measured the dependency of mass flow rate on the pressure differences. He also reported the occurrence of multiple expansion–compression waves in the divergent section.

Lin and Gadepalli (2009) used the continuum equations with no-slip and slip boundary conditions and simulated gas flows through micronozzles. They suggested a correlation between nozzle specific impulse, throat diameter, and the flow Reynolds number. They also examined the effect of different gases on the value of nozzle specific

impulse. Titove and Levin (2007) proposed a collision-limiter method, i.e., equilibrium direct simulation Monte Carlo (eDSMC), to extend the DSMC simulations to high pressure small-scale nozzle and channel flows. Their simulation captured the compression waves in the nozzle, which were in good agreement with high-order Euler solutions. Xu and Zhao (2007) chose the NS equations subject to slip wall boundary conditions and simulated small-scale nozzle flow subject to different back pressures. They studied the shock structures at low Knudsen number flows. They found that the viscous effect would be the key parameter in shock wave formation within the micronozzle. Louisos et al. (2008) reviewed the key findings obtained from computational studies of supersonic micronozzle flow using both the continuum and kinetic-based techniques. They reported that the combination of viscous, thermal, and rarefaction effects on the microscale flow structure would considerably affect the supersonic flow behavior in micronozzles. They described different aspects of rarefaction effects in nozzle performance. They also reported that the thermal non-equilibrium, i.e., the delay in the rotational and vibrational energy relaxations, would reduce the performance in low Reynolds number micronozzle flows. San et al. (2009) studied the size and expansion ratio effects on the micronozzle flow field behavior solving the 2D augmented Burnett and the NS equations. They reported small differences in the solutions of low Knudsen number flows subject to either slip or no-slip boundary conditions. Sun et al. (2009) investigated the flow and temperature fields in free molecular micro-electro-thermal resist jet (FMMR) using a coupled DSMC and finite-volume method. They studied the effect of inlet pressure. Their results showed that the temperature of solid area would change drastically imposing different inlet pressure conditions.

The main objective of the current study is to provide a deeper understanding of the flow behavior in the micro/nanoscale converging–diverging nozzles. We use DSMC to confidently model a wide range of rarefaction flow regimes through the micro/nanoscale nozzles. We investigate the effects of back pressure, Knudsen number, and gas–surface interaction on the nozzle flow behavior. We also describe the correct position, where the back pressure boundary conditions, should be imposed at the nozzle exit. We have already validated our basic DSMC solver through simulating different micro/nanoscale geometries (Roohi et al. 2009; Roohi and Darbandi 2009). However, to analyze the nozzle flow more robustly, our basic DSMC solver has been suitably extended to unstructured grid applications. Using the compressible OpenFOAM solver (2009), we also compare the results of DSMC with the NS solutions whenever applicable.

2 The DSMC method

2.1 Basic algorithm

DSMC is a numerical approach to solve the Boltzmann equation based on direct statistical simulation of the molecular processes described by the kinetic theory (Bird 1994). It is categorized as a particle method in which each particle represents a large bulk of real gas molecules. The physics of gas is modeled through uncoupling the particles motion and their collisions. The implementation of DSMC needs breaking down the computational domain into a collection of grid cells. After fulfilling all the required molecular movements, the collisions between particles are simulated in each cell independently. In the current study, variable hard sphere (VHS) and Larsen–Borgnakke (LB) collision models are used and the collision pair is chosen based on the no-time counter method (Bird 1994). The main steps in DSMC method are to set up the initial conditions, to move and index the particles, to collide particles, and to sample the particles within cells to determine the thermodynamic properties such as temperature, density, and pressure. In addition, the communication between cells are required as one particle moves from one cell to another one. Therefore, each particle must reside in one individual cell for a sufficient long period to ensure binary collisions and to obtain the correct local molecular velocity distribution. Consequently, the DSMC time step should be smaller than the mean collision time, defined as λ/V_{mp}, where V_{mp} is the most probable speed. As a result of this restriction, the particles do not cross more than one cell during one time step and this provides suitable communication between cells.

Following Wang and Li (2004), we use the 1D characteristic theory to apply the inlet/outlet pressure boundary conditions. For a backward-running wave, we consider $du/a = -d\rho/\rho$, where $a = \sqrt{dp/d\rho}$ is the speed of sound and p and ρ are pressure and density, respectively. Applying this definition to a boundary cell, it yields

$$(\rho_o)_j = \rho_j + (p_o - p_j)/a_j^2 \qquad (1)$$

Using the perfect gas law, the outlet temperature can be calculated from

$$(T_o)_j = p_o/(\rho_o)_j R \qquad (2)$$

The subscripts o and j denote the quantities at the outlet boundary and the jth cell adjacent to the outlet boundary, respectively. Using the characteristic wave equation, the velocity can be obtained from

$$(u_o)_j = u_j + (p_j - p_o)/(\rho_j a_j) \qquad (3)$$

For a subsonic pressure driven flow, the inlet velocity is also unknown and must be extrapolated from the interior domain. Then, the inlet velocity is calculated from

$$(u_{in})_j = u_j + (p_{in} - p_j)/(\rho_j a_j) \qquad (4)$$

In addition, the density at the inlet is calculated from the equation of state as follows:

$$(\rho_{in})_j = p_{in}/(RT_{in}) \qquad (5)$$

The velocities of the reflected particles are randomly attributed according to the one-half range Maxwellian distribution, which is determined by the wall temperature. The reflection from a symmetry boundary was considered elastic. That is the normal velocity component is being reversed while the tangential component remains unchanged.

2.2 Subcells arrangement

Each DSMC cell is further divided into a few subcells. Then, possible collision pairs are randomly selected from the same subcell. As shown in Fig. 1, we can divide each cell or triangle into three or four subcell arrangements. The three-subcells arrangement considers the possibility of collision between two particles with the farthest distance in the same subcell, i.e., particles located near two cell vertices. Therefore, the collisions may not be truly physical. Alternatively, four-subcells arrangement can result in more accurate solutions because it considers the possibility of collision among the closer particles. In addition, our simulations showed that the computational time would increase up to 25% if we used the three-subcells arrangement for the same number of grid cells.

2.3 Initial particle distribution

In DSMC, particles are initially distributed in a random manner at the first step. For an arbitrary triangular mesh, we use two different approaches to distribute the particles. In the first one, we determine the particle axial position (X) from

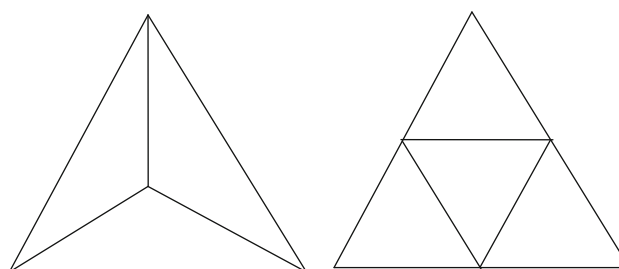$$X = \min(x_1, x_2, x_3) + \alpha \\ \times \max(|x_2 - x_1|, |x_3 - x_2|, |x_1 - x_3|), \qquad (6)$$

Fig. 1 Three-subcells (*left*) and four-subcells (*right*) arrangements for a triangular mesh

where x_1, x_2, and x_3 are the x-coordinates of cell vertices and $0 \leq \alpha \leq 1$ is a random number. Next, we find the intersections (y_{is1}, y_{is2}) of a vertical line, which crosses two sides of one triangle. Moreover, the Y position of particle is determined from

$$Y = \min(y_{is1}, y_{is2}) + \mu \times |y_{is2} - y_{is1}|, \tag{7}$$

where $0 \leq \mu \leq 1$ is another random number. Our experience showed that this approach could result in a non-uniform distribution and the particles may congest near one of the vertices of the cell, see Fig. 2a. This distribution results in a longer computational time to converge. However, the second approach uses alternative positions as follows:

$$X = \alpha \times x_1 + \mu \times x_2 + (1 - \alpha - \mu) \times x_3 \tag{8}$$

$$Y = \alpha \times y_1 + \mu \times y_2 + (1 - \alpha - \mu) \times y_3, \tag{9}$$

where y_1, y_2, and y_3 are the y-coordinates of cell vertices and $(\alpha + \mu) < 1$. As shown in Fig. 2b, this formula results in more uniform distributions within the sub cells.
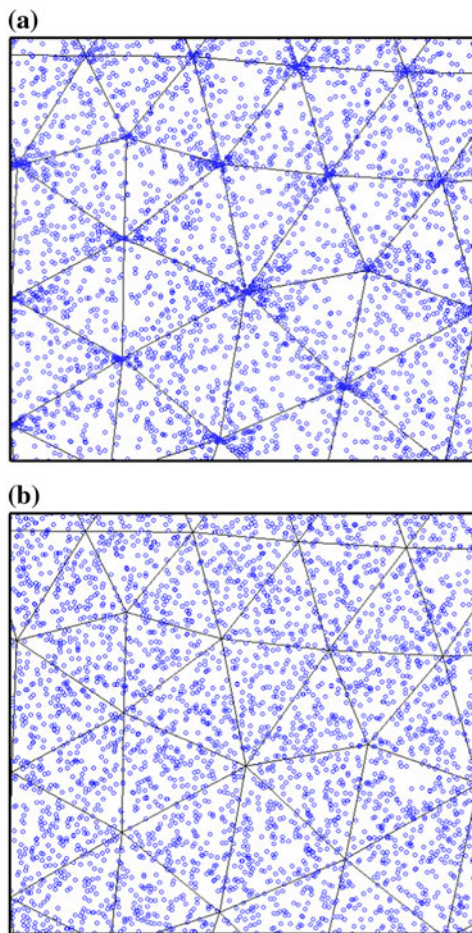

Fig. 2 Two types of initial particle distributions including **a** a non-uniform distribution (using Eqs. 6 and 7) and **b** a uniform distribution (using Eqs. 8 and 9)
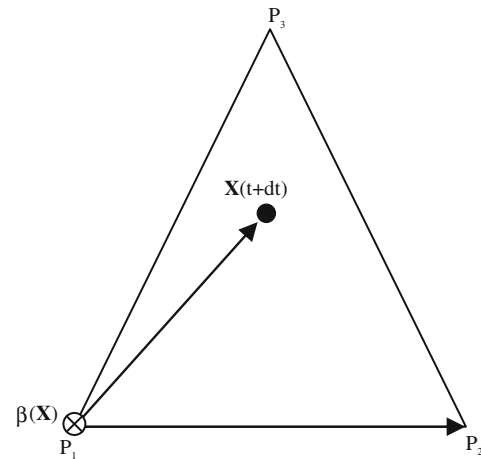

Fig. 3 Schematic of a P2L test applied in our unstructured particle tracking algorithm

2.4 Particle tracking algorithm

As is known, it is straightforward to find the new position of particles in structured cells because there are simple algebraic relations between the particle position and the cell geometry. However, a direct search within mesh may be required to determine the new position of particles in an unstructured mesh. We use a "direct search" algorithm called Zhou and Leschziner (ZL) (Zhou and Leschziner 1999) algorithm in our DSMC solver. This algorithm is straightforward and needs a little more computational time but may search in a great number of cells. It benefits from the "particle to left" (P2L) idea, see Fig. 3. The P2L states that if a particle is located in the left sides of all cell faces it would be located inside the cell. In other words, the particle is inside the cell if the cross product of the triangle edge vector ($\mathbf{P_iP_{i+1}}$) and the connecting vector between the particle position and the vertices of the edge ($\mathbf{P_iX}(t + dt)$) is positive. This cross product ($\boldsymbol{\beta}(\mathbf{X})$) should be calculated for all the edges of cell unless resulting in a negative value. Then, the ZL algorithm must be performed for different layers of neighboring cells.

3 The Navier–Stokes solution

The NS equations are typically valid if the slip velocity and temperature jump boundary conditions are suitably applied when $0.001 < Kn < 0.1$. In order to evaluate the accuracy of the NS equations in the solution of rarefied gas flows, we use OpenFOAM (2009) to simulate micronozzle flow. The OpenFOAM, Open Field Operation and Manipulation, is a programmable CFD toolkit licensed under the GNU General Public License. The OpenFOAM distribution contains numerous solvers and utilities and covers a wide range of

problems. It is a finite-volume package designed to solve systems of differential equations in arbitrary 3D geometries. It uses a series of discrete C++ modules. We use "Rho-Centralfoam" solver to simulate subsonic–supersonic nozzle flows. RhoCentralfoam is an explicit density-based solver for simulating the viscous compressible flow of perfect gases. It benefits from a Godunov-like central-upwind scheme. The space discretization has a second-order accuracy based on the reconstruction of the primitive variables of pressure, velocity, and temperature. Time integration employs the first-order (forward) Euler scheme. For more details about this solver, see Ref. O'Hare et al. (2007). In order to consider rarefaction effects on the walls, we use the first-order velocity slip and temperature jump boundary conditions on the walls as follows:

$$u_{\mathrm{g}} - u_{\mathrm{w}} = \frac{2 - \sigma_u}{\sigma_u} Kn \left(\frac{\partial u}{\partial n} \right)_{\mathrm{w}} \tag{10}$$

$$T_{\mathrm{g}} - T_{\mathrm{w}} = \frac{2 - \sigma_{\mathrm{T}}}{\sigma_{\mathrm{T}}} \left(\frac{2\gamma}{\gamma + 1} \right) \frac{Kn}{Pr} \left(\frac{\partial T}{\partial n} \right)_{\mathrm{w}}, \tag{11}$$

where n indicates the normal direction, the subscripts w and g stand for wall and gas adjacent to wall, γ is the specific heat ratio, Pr is the Prandtl number, σ_u is the tangential momentum accommodation coefficient, and σ_{T} is the thermal accommodation coefficient. We consider both of these coefficients unity in studying diatomic nitrogen gas flow. Meanwhile, Agrawal and Prabhu (2008) have shown that the value of tangential momentum accommodation coefficient would be 0.926 for monatomic gas studies. Alexeenko et al. (2002) showed that the dependency of nozzle flow solution to the accommodation coefficient is quite weak if this coefficient increases from 0.8 to 1.

4 Results and discussion

In this section, we present our DSMC results and the NS solutions for the micro/nano-nozzle flows and evaluate the accuracy of the NS solutions for simulating the rarefied internal gas flows. In this regard, we first describe our defined test cases. Second, we validate our DSMC solver for supersonic flow through micronozzles. We also perform grid independency test and compare the DSMC results with the NS solutions. Next, we study the effects of back pressure and gas–surface interaction on the flow behavior and temperature distribution in micronozzles. Eventually, we consider the physics of high Knudsen number flows through nanonozzles.

4.1 Test cases

Figure 4 shows the geometry of chosen micronozzle and the distributed triangular unstructured grid. Considering a symmetric flow, we only study one-half of the solution domain geometry. In all cases, we consider nitrogen as the working fluid. In the simulation of micro/nanoscale flows, the correct implementations of the inlet and outlet boundary conditions play pivotal roles in the numerical achievements; see Refs. Roohi et al. 2009; Roohi and Darbandi 2009; Darbandi and Vakilipour 2007; Vakilipour and Darbandi 2009; Darbandi and Vakilipour 2009. In simulating the subsonic inlet flow with DSMC, we specify pressure and temperature at the inlet. The velocity and number density magnitudes are calculated from Eqs. 4 and 5, respectively. For the supersonic outlet case, all the quantities are extrapolated from the interior domain. For the subsonic outlet case, we should specify pressure at the outlet. Density, temperature, and velocity magnitudes are calculated from Eqs. 1 to 3. We will show that it is necessary to add a buffer zone at the end of nozzle in order to simulate the subsonic flow at the outlet more accurately. For the NS solution of supersonic micronozzle flow, we specify total pressure, pressure and temperature magnitudes at the inlet and we do not specify any property at the outlet. We adjust the total pressure in a manner that the inlet velocity is identical for both the NS and DSMC solvers. Therefore, the boundary conditions for both solvers are identical. The time step is adjusted in a manner to be smaller than the mean collision time and to satisfy a CFL number smaller than one. The CFL number is defined in terms of V_{mp}. The values of mass flow rate at the inlet and outlet are monitored until achieving negligible differences between two subsequent time steps.

We study the effects of back pressure, Knudsen number, and gas–surface interaction on the micro/nanoscale nozzle flow behavior. Table 1 provides a summary of the current investigated test cases. Cases 1–5 correspond to micronozzle flow and cases 6–7 consider the flow in nanonozzle. Case 1 studies a supersonic flow. Cases 2–5 consider the effects of back pressure. We simulate cases 1–6 imposing both viscous and inviscid wall boundary conditions. For cases 1–5, the throat height H_{t} is 15 μm and $Kn_{\mathrm{in}} = 7.5 \times 10^{-4}$. For cases
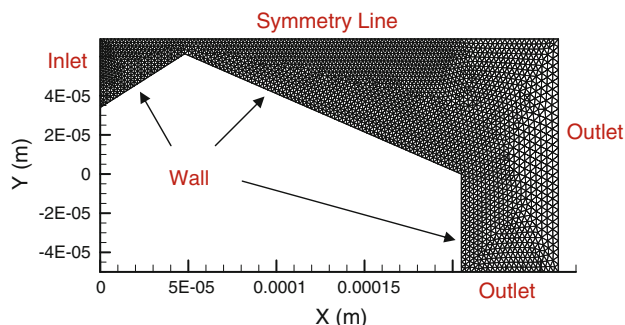

Fig. 4 The unstructured triangular grid distribution in the computational domain and the imposed boundary conditions

Table 1 Details of the investigated micro/nano nozzle test cases

Case	P_{back} (kPa)	$\overline{Kn}_0$ $(\times 10^3)$		Re_t
		Diffusive	Specular	
1	–	8.01	9.67	406
2	7	3.24	6.92	260
3	15	1.95	1.63	269
4	25	1.93	1.13	257
5	35	1.01	0.91	247
6	–	521	382	0.05
7	20	244	–	0.04

6–7, $H_t = 40$ nm and $Kn_{in} = 0.153$. In all simulations, $P_{in} = 1$ atm and $T_{wall} = T_{in} = 300$ K. The Reynolds number ($Re_t = \rho_t c_s H_t / \mu$), based on the nozzle throat height and the speed of sound (c_s) is only reported for the viscous wall cases. The nozzle thrust is calculated using $F_t = \dot{m}u$, which is proportional to the throat Reynolds number because $\dot{m} = Re_t \mu_0 h$. Therefore, the Reynolds number at the

throat, as reported in Table 1, is an indicator of the nozzle propulsion performance.

4.2 Validation and grid independency tests: case 1

We set 20 molecules in each cell at time zero. Figure 5 shows the effect of the average number of simulated molecules per cell (MPC) on the pressure and Mach number distributions at the centerline and the pressure and Mach profiles at the nozzle outlet. The solutions are predicted for case 1 considering MPC = 3, 4, 8, and 17. It is observed that the accuracy of the solutions remains almost unchanged if we increase MPC from 8 to 17. This observation was also confirmed using the rule proposed by Bird (2007), who indicated that the optimum number for the simulated particles would be around 7. Since the flow velocity is relatively high in the divergent sections, we can obtain an accurate solution considering only a few numbers of simulated particles in each cell. There are slight dependencies on the pressure distributions in $X/L = 0.0$–0.3 considering different MPC magnitudes. These differences are due to a low

(a) centerline pressure distribution

(b) centerline Mach distribution

(c) outlet pressure profile
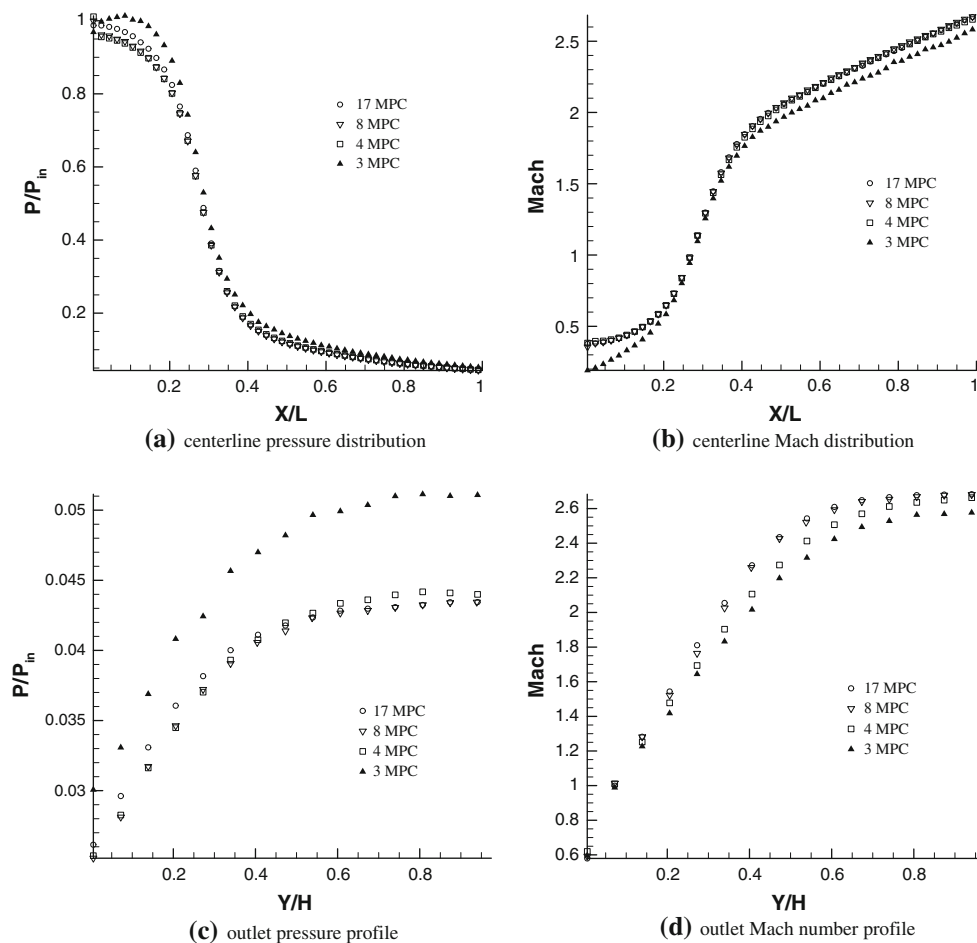
(d) outlet Mach number profile

Fig. 5 Effect of the average number of MPC on the centerline pressure and Mach number distributions and the outlet pressure and Mach number profiles
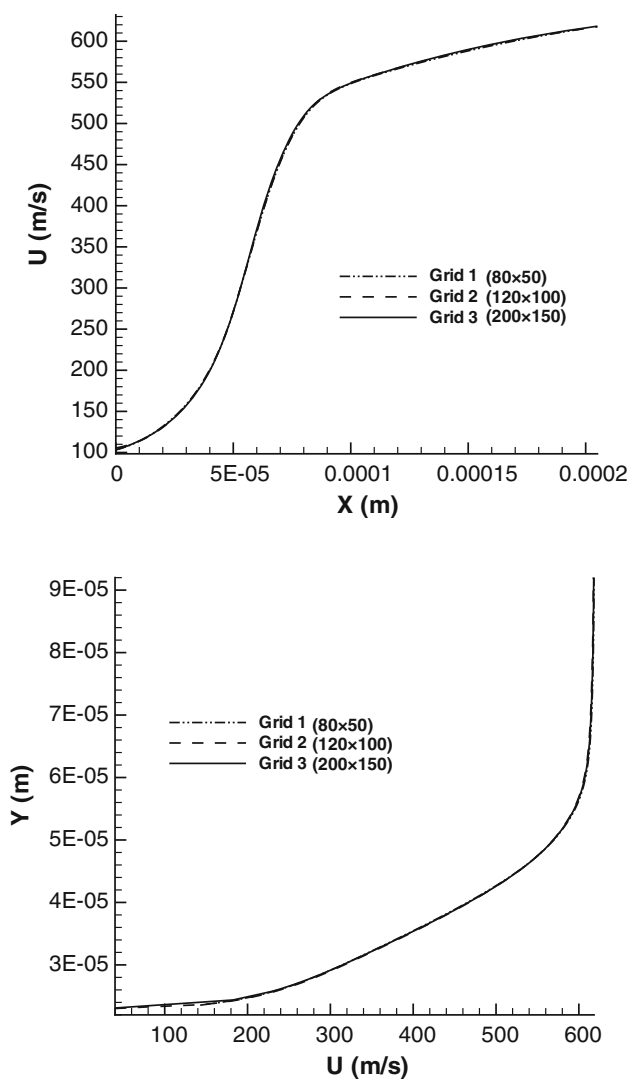
Fig. 6 The effect of grid size on the centerline velocity distribution (*left*) and the velocity profile at the outlet (*right*) using the NS solver, case 1

Fig. 7 The effect of grid size on the DSMC solution for the velocity slip (*left*) and temperature jump (*right*) and comparison with the NS solutions, case 1

speed flow near the inlet of nozzle. We previously observed that the pressure distribution would remain unchanged if we increase the MPC from 12 to 17. Le et al. (2006) also reported similar conclusions about the effects of MPC value on the accuracy of DSMC solution. We will use MPC $\geq$ 25 to perform our DSMC calculations.

At the beginning, we perform grid studies to determine suitable cell sizes for the NS and DSMC solvers. In the first stage, we choose three different grid sizes of Grid 1 (80 × 50), Grid 2 (120 × 100), and Grid 3 (200 × 150) to solve the NS equations using the OpenFOAM solver. Figure 6 shows the calculated centerline velocity distributions and the velocity profiles at the nozzle outlet for case 1. Indeed, the solutions are identical and the grid size has no impact in improving the solution accuracy in either *x* or *y* directions. In the next stage, we present grid independent
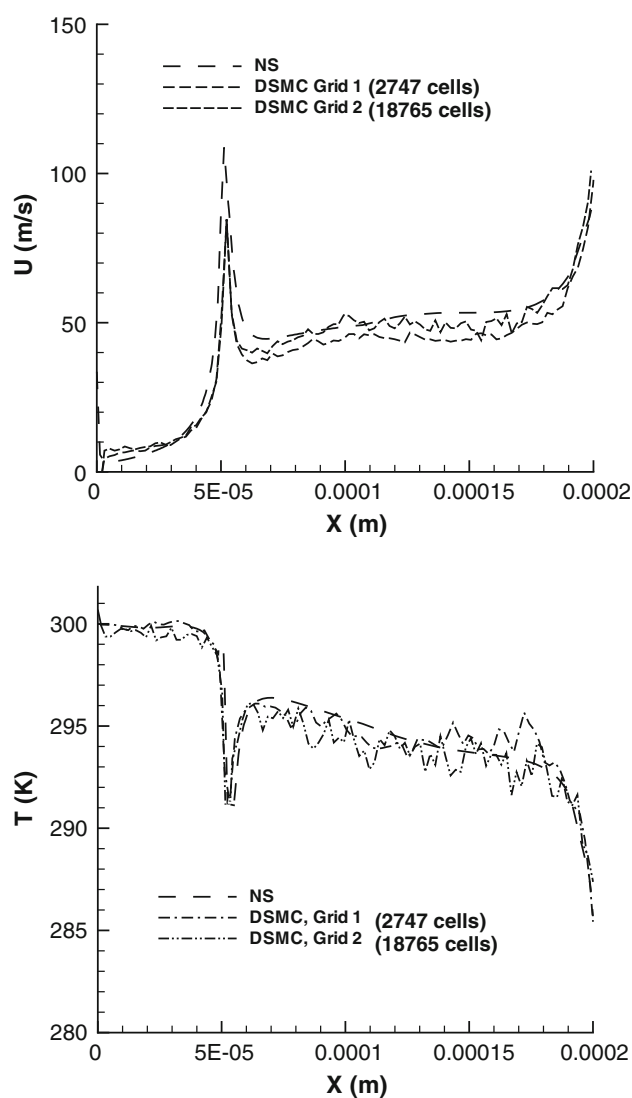
study for our extended DSMC solver using two grid resolutions of 2,747 (Grid 1) and 18,765 (Grid 2) unstructured cells. Since the region in vicinity of the wall is the most sensitive part with respect to the cell sizes, we study the velocity slip and temperature jump distributions along the nozzle wall. The results are shown in Fig. 7 and are compared with the NS solution. In the DSMC simulation, we should keep the size of the largest cells less than the local mean free path in the direction where the gradients of the flow are high, which is in the transversal direction (Le et al. 2006; Cai et al. 2000; Shen et al. 2003). The features of unstructured grid facilitate suitable grid refinement with the local mean free path variations. It should be noted that the size of cells in grid 2 is smaller than the mean free path in the transversal direction. The two DSMC solutions presented in Fig. 7 are close to each other; however, the solution for

grid 2 is closer to the NS solution. Meanwhile, the scattering observed in the DSMC solutions are due to a relatively lower speed of flow near the wall. We observe slip in the velocity distribution and jump in the temperature distribution right at the beginning of the divergent part of nozzle. Agrawal et al. (2005) also reported similar behavior in solving rarefied flow in channels geometry with sudden expansion or contraction. As is indicated by the reference, these discontinuities originate from the gas compressibility effects.

The next step, we compare the results of our unstructured solver with those of our structured DSMC code. Figure 8 shows Mach and temperature contours for both structured ($100 \times 30 = 3{,}000$ cells) and unstructured (2,747 cells) grid distributions. As is seen, there is slight difference between the two solutions at the convergent part, where the flow speed is quite low. It is an indication of flow sensitivity to the number and shapes of cells there. However, the contours of two grids show more similarity in high speed flow region in the divergent section. Similarly, the smoothness and low scattering of the DSMC solution at the centerline is due to experiencing a relatively high speed flow there.

Figure 9 shows different contours for the flow variables including Mach, density, temperature, and velocity using
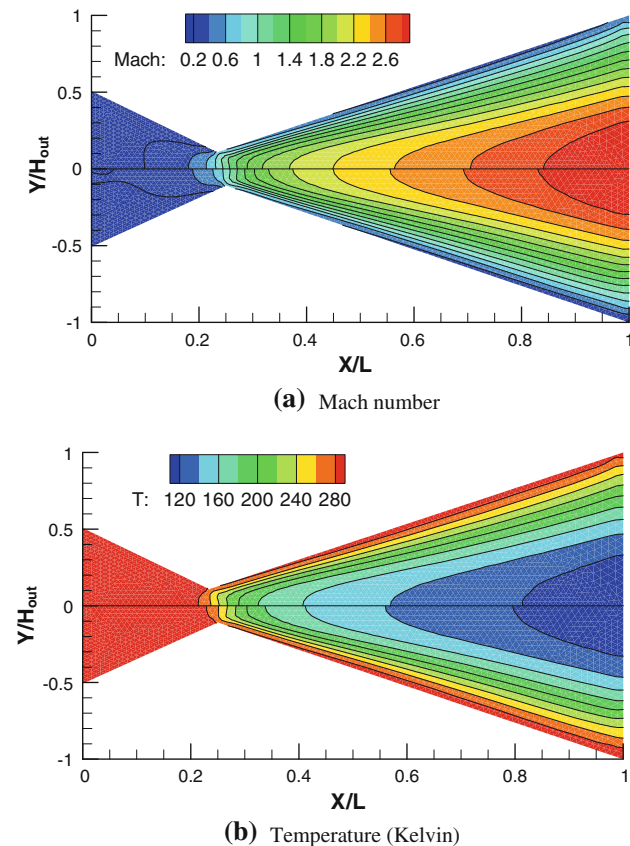

(a) Mach Contours

(b) Density contours

(c) Temperature Contours

(d) Velocity contours

Fig. 9 Contours of flow variables for the NS (*top zones*) and DSMC (*bottom zones*) simulations in nozzle with a supersonic outflow, case 1

(a) Mach number

(b) Temperature (Kelvin)

Fig. 8 Comparison between structured (*top zones*) and unstructured grid (*bottom zones*) solutions for the nozzle with supersonic outflow, case 1
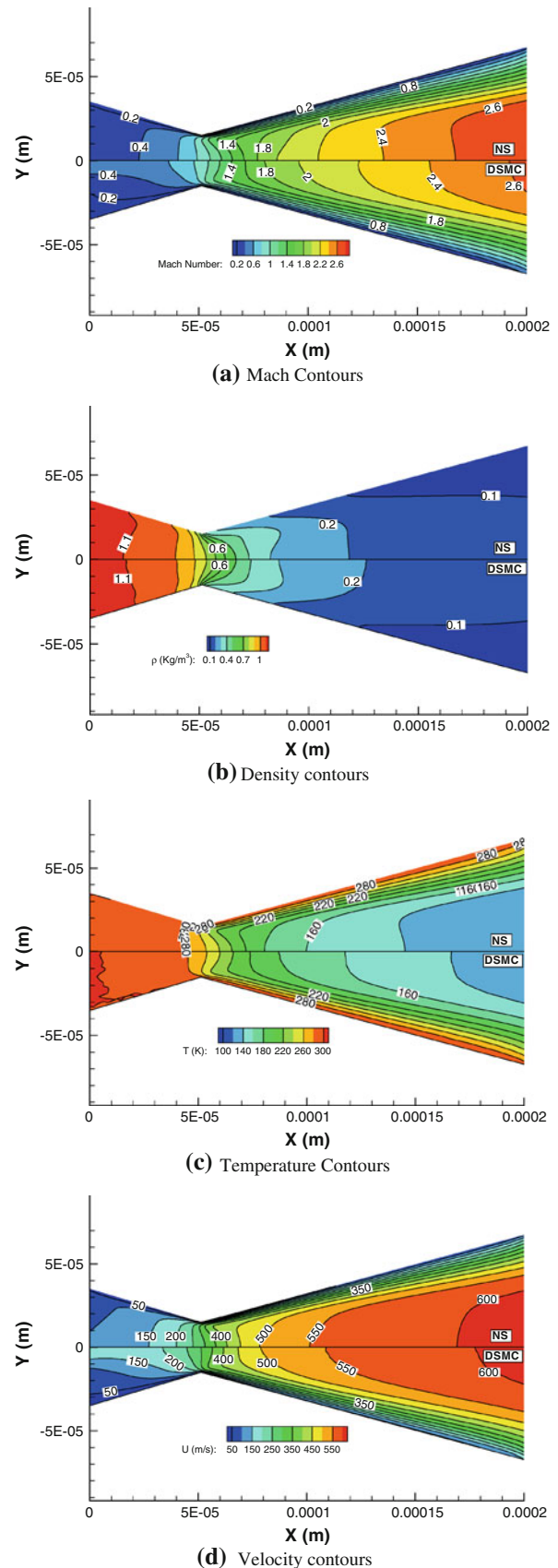
(a) centerline velocity
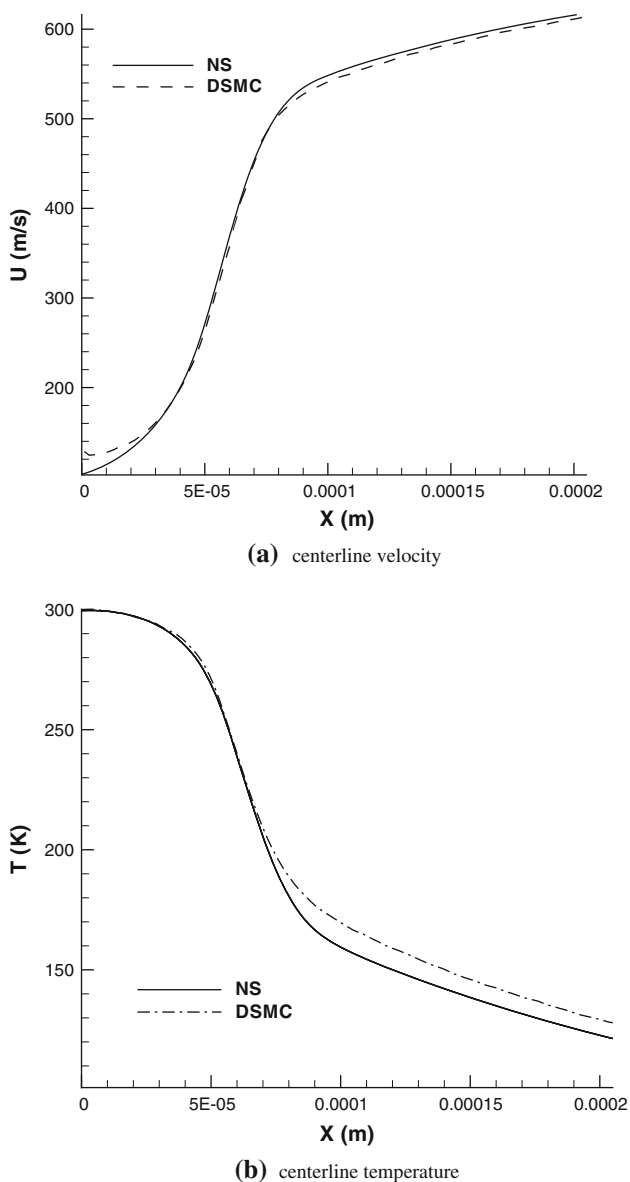

(b) centerline temperature

Fig. 10 DSMC centerline velocity and temperature distributions and comparing them with those of the NS solutions for nozzle with a supersonic outflow, case 1

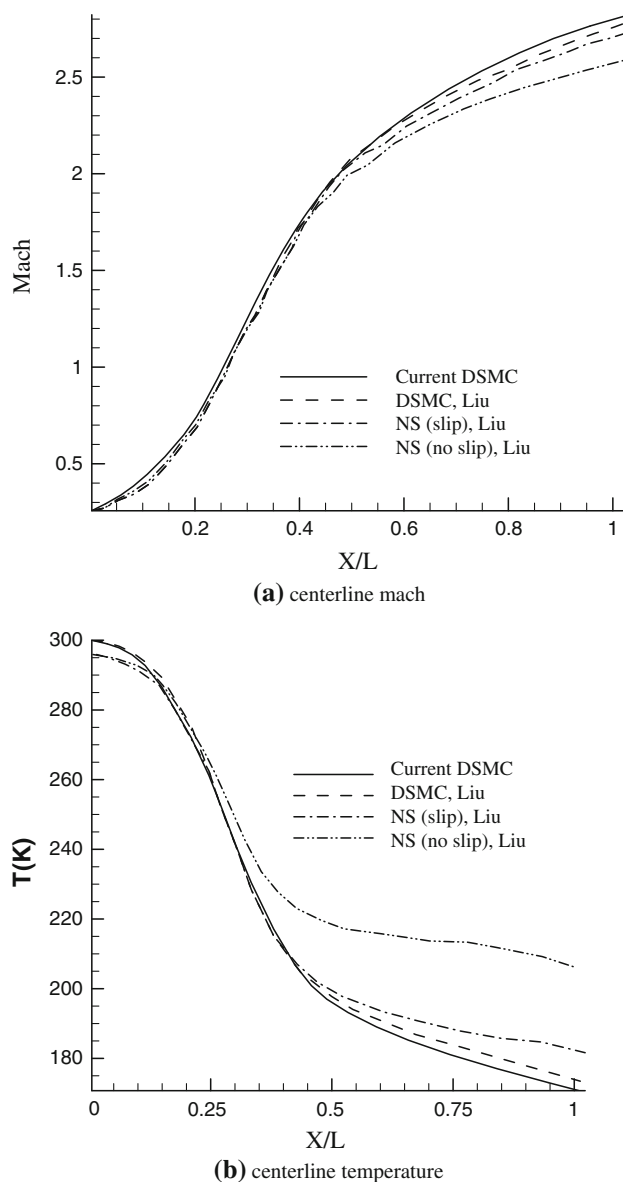**(a)** centerline mach

(b) centerline temperature

Fig. 11 The current centerline Mach and temperature distributions and comparison with the DSMC and NS (with and without slip boundary conditions) solutions (Liu et al. 2006) for a nozzle with a supersonic outflow, case 1

both the NS and DSMC simulations. Figure 10 shows the velocity and temperature distributions at the nozzle centerline using the NS and DSMC simulations. Both the NS and DSMC solutions show similar patterns although the NS solution predicts slightly higher velocity and lower temperature magnitudes at the divergent part of the nozzle.

In the next step, we compare our DSMC solution with those of others. Figure 11 compares the centerline Mach number and temperature distribution derived from the current unstructured DSMC solver with the DSMC and the NS solutions of Liu et al. (2006). The DSMC solutions agree with each other. It should be reminded that Liu et al. (2006) used a grid with 410×140 non-uniform quadrilateral

elements to solve this test case. A good agreement between the current DSMC solution and that of Liu et al. (2006) indicates that the cell employed in the current simulation is fine enough to achieve suitable accuracy. Since the Knudsen number is small in the convergent part, both the DSMC and the NS solutions (subject to slip/jump boundary condition) agree closely there. However, the discrepancy between the NS and DSMC solutions increases as the flow expands and experiences more serious rarefaction in the divergent part. As is seen, the NS solution without applying suitable slip/jump boundary conditions is far incorrect, especially for the temperature distribution.
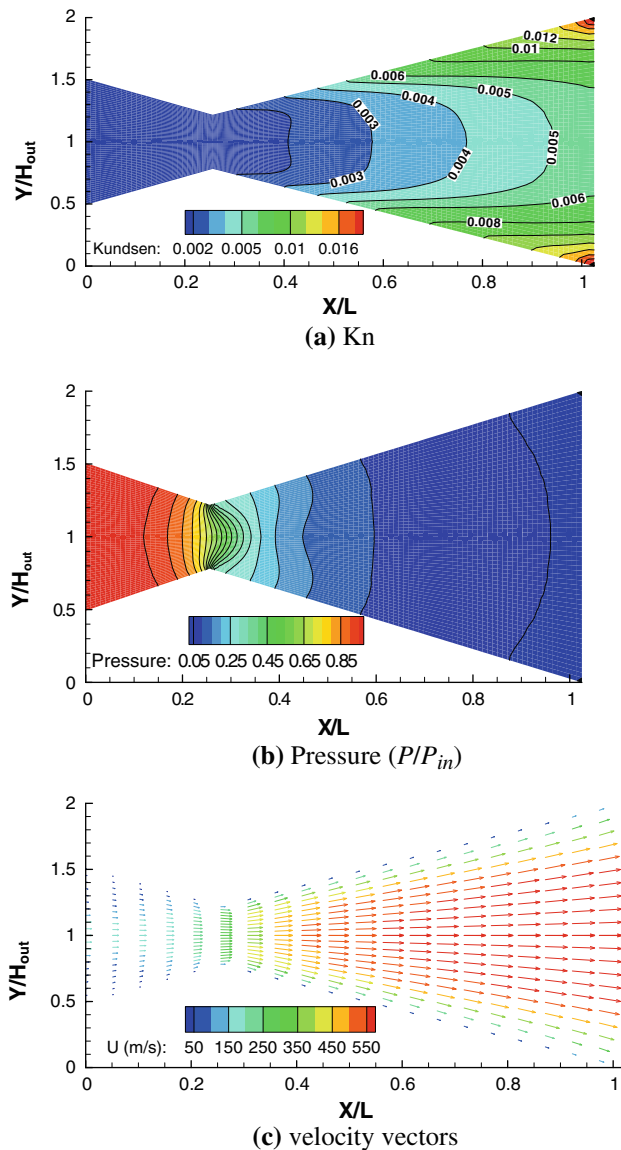
(a) Kn

(b) Pressure (P/P_{in})

(c) velocity vectors

Fig. 12 Knudsen number and pressure contours and velocity vector field for a nozzle with a supersonic outflow, case 1

Figure 12 illustrates two more maps for case 1. Figure 12a shows the Knudsen number contours, defined using the height of nozzle at its outlet ($Kn = \lambda/H_{out}$). It is observed that the gas experiences one-order of magnitude rarefaction as the flow is expanded in the divergent part. The rarefaction is slightly stronger near the nozzle walls since the velocity acceleration due to slip flow and the wall heat transfer reduces the density magnitude. In the vicinity of the nozzle exit, the impact of flow rarefaction is significant again. As indicated in Table 1, the average outlet Knudsen number is about 8.01×10^{-3}, which is lower than the slip flow limit. However, the local Knudsen number at the outlet increases well above the slip flow limit, see Fig. 12a. This description can provide good reason about the differences between the NS and DSMC solutions observed in Figs. 9, 10, 11.

Figure 12b shows the pressure contours. It is observed that the pressure distribution is non-uniform along the y-direction, i.e., $dp/dy > 0$ in the convergent part and $dp/dy < 0$ in the divergent part. Uribe and Garcia (1999) have also reported non-uniform pressure distribution in the rarefied Poiseuille flow. Figure 12c shows the velocity vector field. We can clearly observe a rapid expansion of the rarefied flow in the divergent part.

4.3 Effects of back pressure

4.3.1 Role of boundary layer

In this section, we study the effects of back pressure on the flow behavior in the nozzle. Figure 13 shows Mach contours for the back pressures of 35, 25, 15, and 7 kPa. In all cases, the flow is choked at the throat. As is seen, there are high Mach number cores in the divergent part. The number of such Mach cores increases and then decreases as the back pressure decreases. As is seen, the strength of these Mach cores decay as the flow approaches the outlet. Since the pressure close to the exit region of the nozzle is not uniform, it is mandatory to apply the back pressure at the exit of a buffer zone added to the outlet of nozzle. As the back pressure decreases, the first core moves farther from the throat. It is observed that the separated flow covers a considerable part of the divergent section. The height of the unseparated section is approximately equal for the three first cases. Therefore, it is normal to assume that the flow passes through a conduit with approximately a constant height rather than passing through a diverging section, see Fig. 13a–c. This causes an overall reduction in the Mach number at the nozzle exit and decreases the generated thrust. The Mach contours in Fig. 13d are similar to a full supersonic case; see Fig. 8a, except near the nozzle outlet. The reason for this similarity is that the average exit pressure for full supersonic case is 4.5 kPa, which is quite close to 7 kPa.

Xu and Zhao (2007) solved the NS equations and studied the shock wave structures at low Knudsen numbers in micronozzle flows subject to different back pressures. Comparing our results with theirs, we observe Mach cores in regions much farther from the walls. This is due to a stronger influence of the viscosity/rarefaction impact in high Knudsen number flows simulated here. The core regions should disappear following a series of oblique/bow shock formations. The viscosity effects do not permit the shock waves to approach the wall; therefore, a series of high Mach number regions would appear there. Figure 14 shows the distributions of the centerline Mach number under vacuum and four different back pressures of 7, 15, 25, and 35 kPa. As shown in this figure, the early bow shocks reduce the Mach number slightly less than unity. Then, the flow experiences a series of expansion/compression waves along the nozzle.
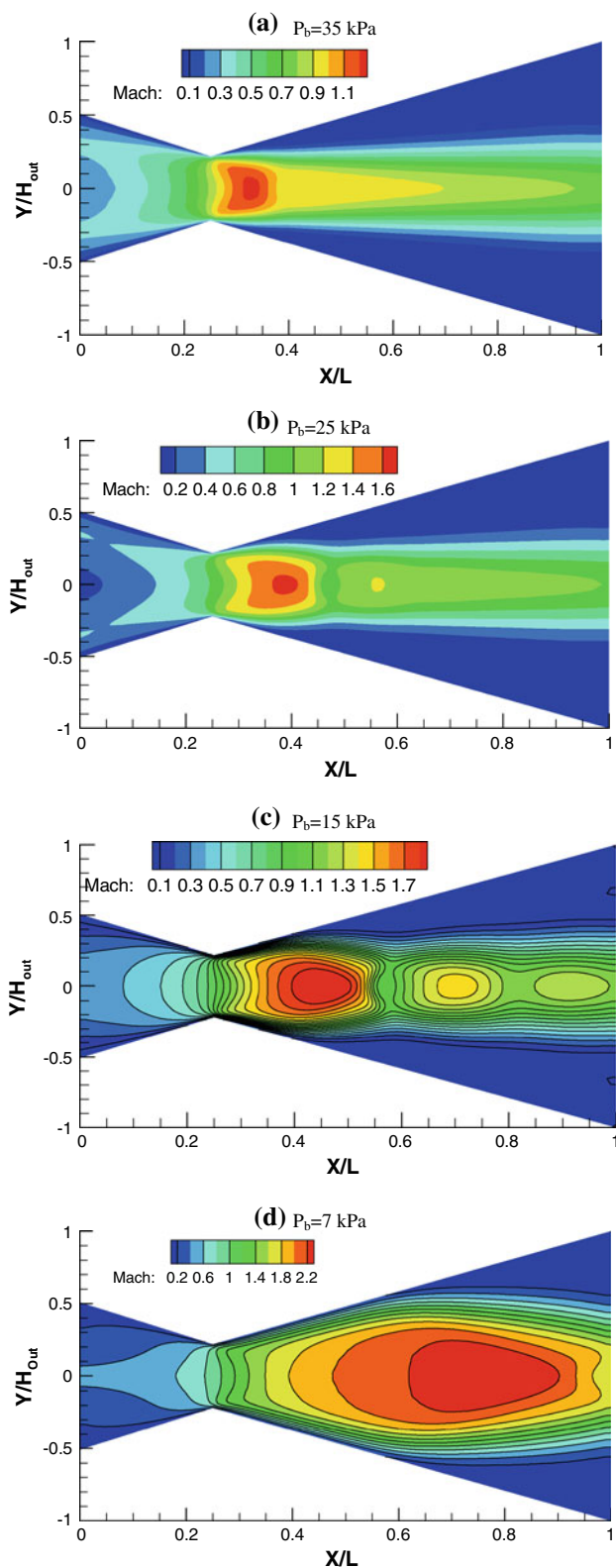
Fig. 13 Mach number contours in nozzle at different back pressures and with a subsonic outflow, cases 2–5
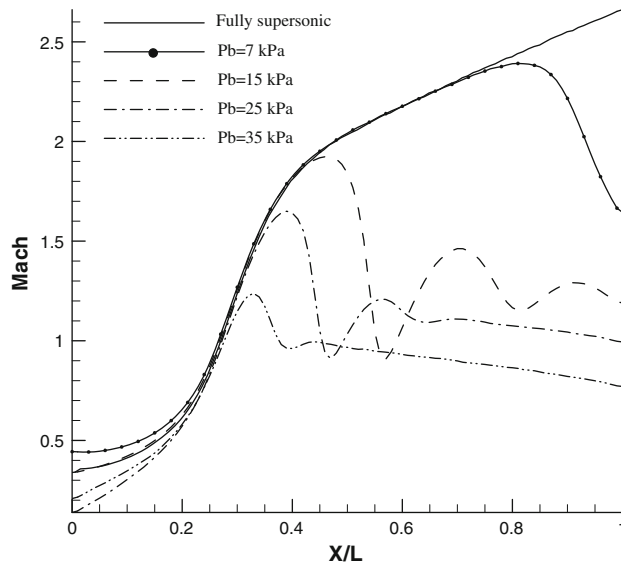

Fig. 14 Centerline Mach number distribution in a nozzle with subsonic and supersonic outflow, cases 1–5

4.3.2 Specular walls

In DSMC, the viscosity is simulated via intermolecular and gas–wall collisions. To study the effects of wall boundary layer (viscosity) on the shock wave structures, we treat the gas–wall interactions in a specular manner. Figure 15 shows Mach number maps for the same back pressures considered in Fig. 13, however, this time we impose specular wall conditions. In fact, our goal is to study the gas–wall interactions on the shock wave structures in the nozzle. Figure 15a shows that a series of weak bow shocks appear right after the throat section. The shock is normal to the walls and to the flow direction. The flow becomes subsonic in the rest of nozzle. Again, we observe separation near the wall. This is due to the fact that the flow in the core region is still viscous. If we decrease the back pressure further, the shock moves closer to the outlet section and the separation region diminishes. If the back pressure decreases to 7 kPa, the shock will move outside the nozzle and will become oblique. Figure 16 shows Mach number distribution at the centerline for the studied cases. Comparing this figure with Fig. 14, we can conclude that the appearance of expansion–compression waves is due to wall viscous effects.

In Table 1, there are two columns of data for the average Knudsen number at the outlet. The first column is for viscous (diffusive) wall and the second one is for the inviscid (specular) wall simulations. Since Knudsen number inversely depends on the density magnitude, a higher outlet Knudsen number ratifies a higher velocity and a lower pressure/temperature there. For example, cases 1 and 2 with
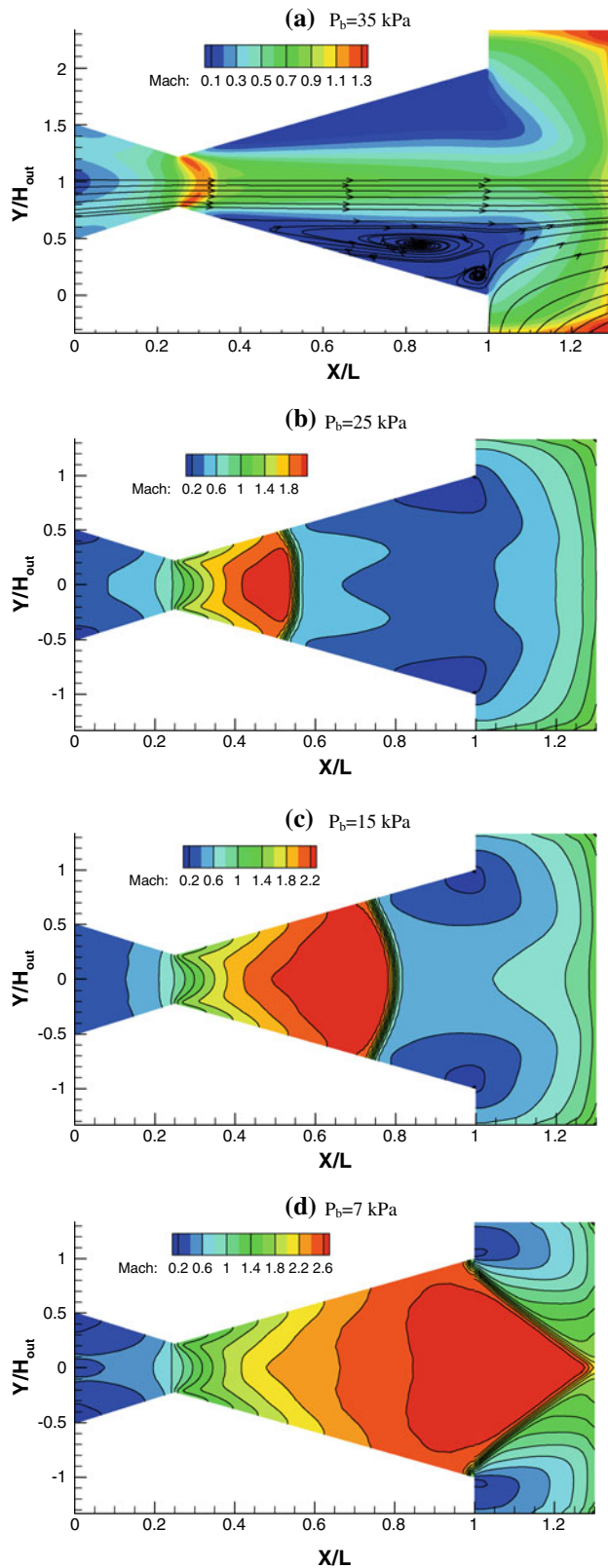
Fig. 15 Mach number contours in a nozzle with inviscid wall imposed at different back pressures and subsonic outflow condition, cases 2–5
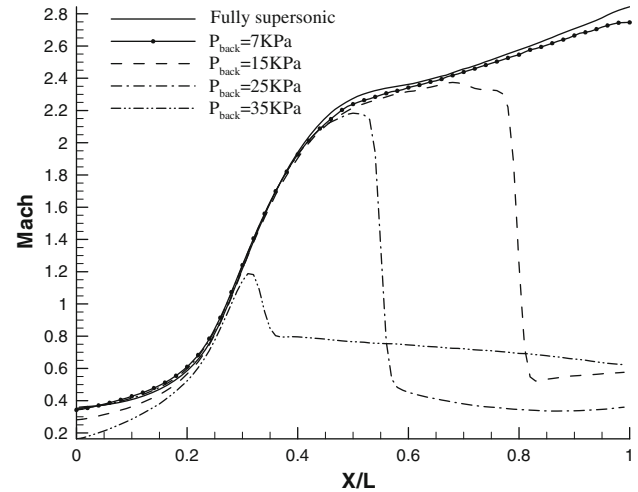

Fig. 16 Centerline Mach number distribution in the nozzle and a comparative study between subsonic and supersonic outflow conditions, cases 1–5

specular wall boundary condition show higher Mach and lower density values at the outlet (see Fig. 16) compared with the same cases imposing diffusive wall boundary condition (see Fig. 14). Therefore, the Knudsen number for cases 1 and 2 with specular boundary condition are higher than the diffusive one. Conversely, the average outlet Mach number for specular condition is lower than that of diffusive walls for cases 3–5. Therefore, the average Knudsen number is lower for the specular walls in cases 3–5.

4.3.3 Temperature profiles

Figure 17 shows temperature profiles at three cross sections of the nozzle with viscous wall effects and imposing the preceding back pressures. Figure 17a shows the temperature profile at one section in the convergent part. There is slight decrease in temperature as the back pressure decreases. The temperature profiles behave in a rather complicated manner in the divergent part due to the mixed effects of rarefaction, thermal boundary layer separation, and rapid conversion of the internal energy to the kinetic one. We observed that the temperature decreases along the nozzle for the fully supersonic flow case. Figure 17b shows a strong decrease in temperature for the case with $P_{back} = 15$ kPa, which is due to a Mach core appearance around $X/L = 0.4$. The case with $P_{back} = 25$ kPa shows slight heating at the centerline due to flow expansion. As is seen, the temperature is constant in the separated region in this frame; however, it increases in Fig. 17c as the flow exits the outlet. The decrease in temperature is stronger for lower back pressures, which is due to having a stronger expansion there.
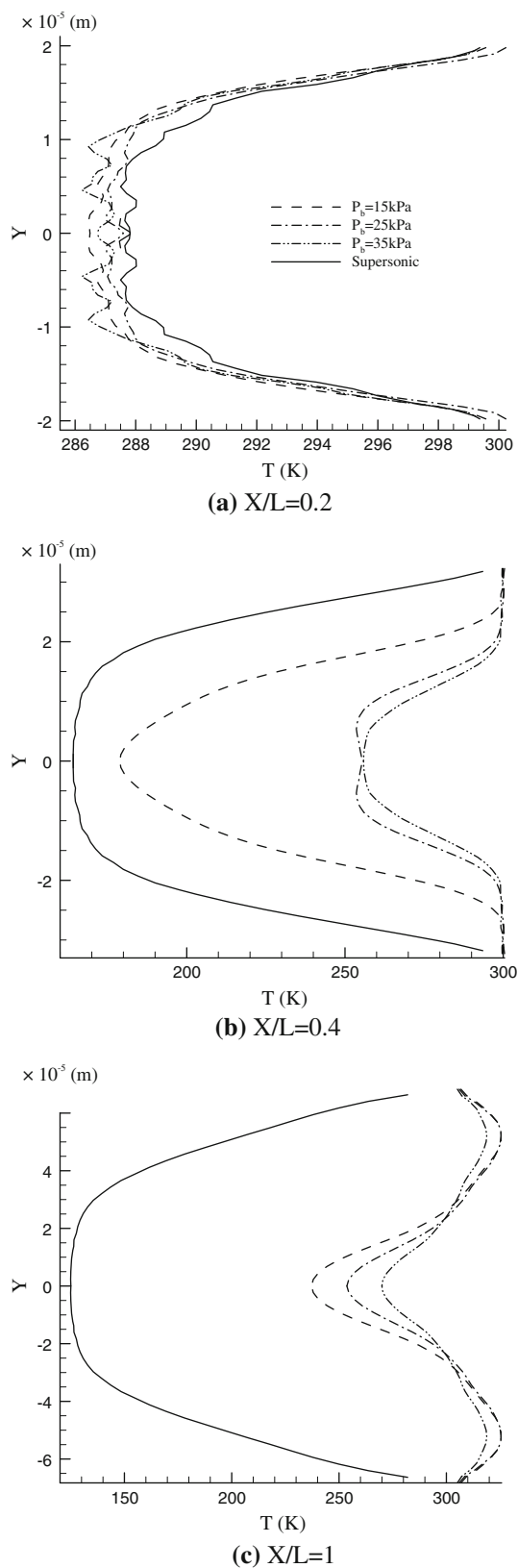
Fig. 17 Temperature profiles at three cross sections in the nozzle applying different back pressures and imposing supersonic and subsonic outflow conditions, cases 1, 3–5

4.4 Flow in nanonozzles

Our investigations show that the past references (Alexeenko et al. 2002, 2006; Louisos and Hitt 2005; Liu et al. 2006; Xie 2007) have not investigated the physics of high Knudsen number flows in nanonozzles. In this section, we study the effects of inlet Knudsen number on the nanonozzle flow field, cases 6 and 7. Figure 18 shows Mach number contours in the nozzle while increasing the inlet Knudsen number from $Kn_{in} = 0.153$ to 0.244. They are obtained under different boundary conditions. Figure 18a refers to a pure supersonic flow in the nozzle considering diffusive (viscous) walls. Figure 18b refers to a pure supersonic flow in the nozzle with specular (inviscid) walls. Figure 18c depicts Mach contours for a nozzle flow with $P_{back} = 20$ kPa, case 7. The average outlet Knudsen number, based on the outlet height, is $Kn_o = 0.521$ in Fig. 18a, $Kn_{out} = 0.382$ in Fig. 18b, and $Kn_{out} = 0.244$ in Fig. 18c. Figure 18a shows a particular behavior, i.e., it is observed that the flow accelerates normally in the divergent section and that the Mach number reaches a value of unity at the buffer zone exit. The acceleration of subsonic flow in the divergent section is quite unexpected. In fact, it is impossible to establish supersonic flow at this high inlet Knudsen number condition. As the Knudsen number increases, the viscous forces dominate and that the dissipation of the kinetic energy becomes sufficiently high. In other words, the flow can neither be choked at the throat nor be accelerated to a supersonic condition in the divergent section. To confirm the role of viscosity, we simulate the same case, however, we impose the specular (inviscid) wall boundary conditions this time; see Fig. 18b. It is observed that the flow is choked at the throat and is accelerated in the divergent part. In addition, a series of bow shocks appears at the divergent part. These bow shocks only change higher supersonic flow conditions to weaker supersonic flow cases.

Figure 18c shows Mach contours for the case with a back pressure of 20 kPa. The flow reaches a maximum Mach number of 0.45 at the throat and is not choked. The subsonic flow decelerates in the divergent part, which is a quite physical behavior for the subsonic flow through a nozzle. Therefore, we conclude that the thick viscous boundary layers prevent the formation of supersonic flow at higher inlet Knudsen numbers in the divergent part of nanonozzles. The observed physics implies that the flow must be subsonic in the nozzle and this requires applying a back pressure at the end of nozzle. It should be mentioned that we observed similar results for flows with higher inlet Knudsen numbers. Based on the current achievements obtained from both the NS and DSMC solvers, the current authors are to extend their NS (Darbandi and Schneider
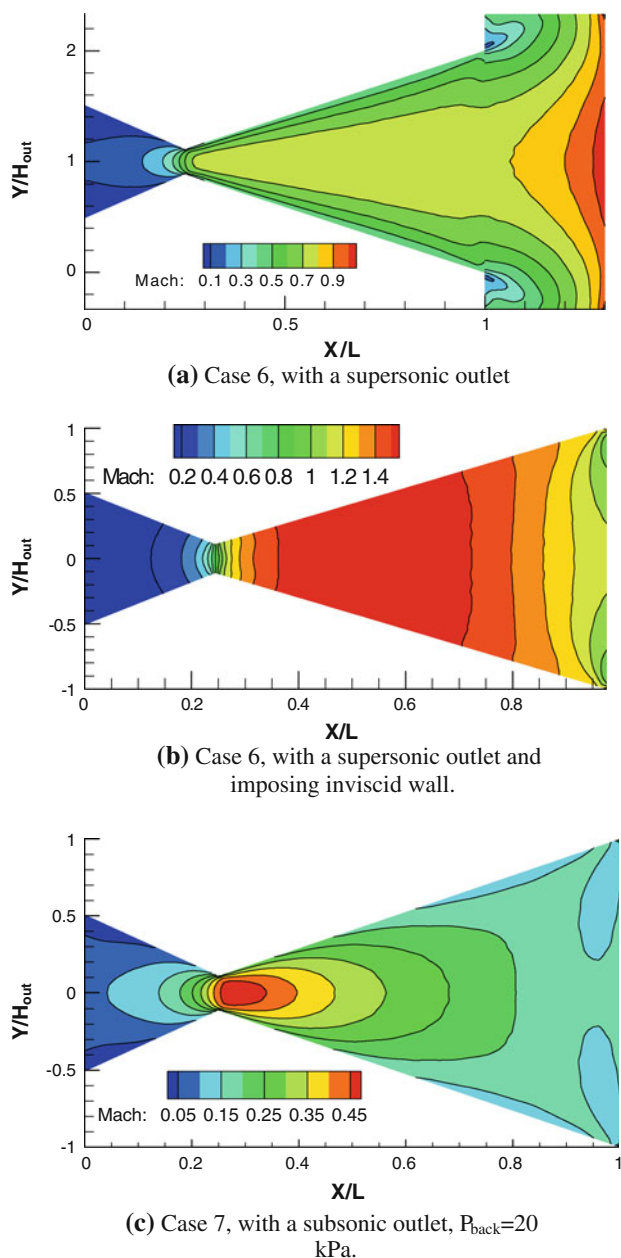
(a) Case 6, with a supersonic outlet

(b) Case 6, with a supersonic outlet and imposing inviscid wall.

(c) Case 7, with a subsonic outlet, P_{back}=20 kPa.

Fig. 18 Mach number contours in nano-nozzles with a constant Knudsen number and imposing in different flow boundary conditions, $Kn_{in} = 0.153$

2000; Darbandi et al. 2008) and DSMC (Roohi et al. 2009; Roohi and Darbandi 2009) solvers to a hybrid NS–DSMC solver.

5 Conclusion

We developed an unstructured DSMC solver and simulated the subsonic and supersonic flows in micro/nanoscale converging–diverging nozzles. It was observed that the mixed impacts of rarefaction, compressibility, and viscous forces

would form the flow behavior in the micro/nanoscale nozzles. The use of a buffer zone far from the nozzle exit allowed eliminating the nonphysical impact of a uniform pressure at the nozzle exit. If we apply a back pressure at the outlet, high viscous forces prevent the formation of normal shocks; alternatively, the regions of high Mach number can appear in the domain. These regions diminish due to formation of bow shocks. In this case, the flow passes through an approximately constant height conduit rather than a divergent nozzle shape because a significant portion of the flow separates near the wall. If we eliminate the flow viscosity from the walls, we observe that the thick bow shocks would appear normal to the walls. Meanwhile, the separated region exists because the main flow is still viscous. We observed that it is impossible to set up supersonic flow in nanonozzles as soon as the inlet Knudsen number exceeds a moderate value. This phenomenon is due to strong viscous force appearances. We showed that it is required to apply a back pressure at the outlet to obtain a physical solution in nanonozzles.

References

Agrawal A, Prabhu SV (2008) A survey on measurement of tangential momentum accommodation coefficient. J Vac Sci Technol A 26:634–645

Agrawal A, Djenidi L, Antonia RA (2005) Simulation of gas flow in microchannels with a sudden expansion or contraction. J Fluid Mech 530:135–144

Alexeenko AA, Levin DA, Gimelshein SF, Collins RJ, Reed BD (2002) Numerical modeling of axisymmetric and three-dimensional flows in microelectromechanical systems nozzles. AIAA J 40(5):897–904

Alexeenko A, Fedosov DA, Gimelshein SF, Levin DA, Collins RJ (2006) Transient heat transfer and gas flow in a MEMS-based thruster. J Microelectromech Syst 15(1):181–194

Bird GA (1994) Molecular gas dynamics and the direct simulation of gas flows. Clarendon Press, Oxford

Bird G (2007) Sophisticated DSMC. Notes prepared for a short course at the DSMC07 meeting, Santa Fe, USA

Cai C, Boyd ID, Fan J, Candler GV (2000) Direct simulation methods for low-speed microchannel flows. J Thermophys Heat Transf 14(3):368–378

Darbandi M, Schneider GE (2000) Performance of an analogy-based all speed procedure without any explicit damping. Comput Mech 26:459–469

Darbandi M, Vakilipour S (2007) Developing consistent inlet boundary conditions to study the entrance zone in microchannels. J Thermophys Heat Transf 21(3):596–607

Darbandi M, Vakilipour S (2009) Solution of thermally developing zone in short micro/nano scale channels. J Heat Transf 131:044501

Darbandi M, Roohi E, Mokarizadeh V (2008) Conceptual linearization of Euler governing equations to solve high speed compressible flow using a pressure-based method. Numer Methods Partial Differ Equ 24:583–604

Le M, Hassan I, Esmail N (2006) DSMC simulation of subsonic flows in parallel and series microchannels. J Fluids Eng 128:1153–1163

Lin CX, Gadepalli V (2009) A computational study of gas flow in a De-Laval micronozzle at different throat diameters. Int J Numer Methods Fluids 59:1203–1216

Liu M, Zhang X, Zhang G, Chen Y (2006) Study on micronozzle flow and propulsion performance using DSMC and continuum methods. Acta Mech Sin 22:409–416

Louisos WF, Hitt DL (2005) Optimal expander angle for viscous supersonic flow in 2D micro-nozzles. AIAA paper 2005-5032

Louisos WF, Alexeenko AA, Hitt DL, Zilić A (2008) Design considerations for supersonic micronozzles. Int J Manuf Res 3(1):80–113

O'Hare L, Lockerby DA, Reese JM, Emerson DR (2007) Near-wall effects in rarefied gas micro-flows: some modern hydrodynamic approaches. Int J Heat Fluid Flow 28:37–43

OpenFOAM (2009) The Open Source CFD toolbox, user guide, version 1.6

Roohi E, Darbandi M (2009) Extending the Navier–Stokes solutions to transition regime in two-dimensional micro-/nanochannel flows using information preservation scheme. Phys Fluids 21:082001

Roohi E, Darbandi M, Mirjalili V (2009) DSMC solution of subsonic flow through micro-nano scale channels. J Heat Transf 131:092402

San O, Bayraktar I, Bayraktar T (2009) Size and expansion ratio analysis of micro nozzle gas flow. Int Commun Heat Mass Transf 36(5):402–411

Shen C, Fan J, Xie C (2003) Statistical simulation of rarefied gas flows in micro channels. J Comput Phys 189:512–526

Sun ZX, Li ZY, He YL, Tao WQ (2009) Coupled solid (FVM)–fluid (DSMC) simulation of micro-nozzle with unstructured-grid. J Microfluid Nanofluid 7(5):621–631

Titove EV, Levin DA (2007) Extension of DSMC method to high pressure flows. Int J Comput Fluid Dyn 21(9–10):351–368

Uribe FJ, Garcia AL (1999) Burnett description for plane poiseuille flow. Phys Rev E 60(4):4063–4078

Vakilipour S, Darbandi M (2009) Advancement in numerical study of gas flow and heat transfer in microchannels. J Thermophys Heat Transf 23(1):205–208

Wang M, Li Z (2004) Simulations for gas flows in microgeometries using the direct simulation Monte Carlo method. Int J Heat Fluid Flow 25:975–985

Xie C (2007) Characteristics of micronozzle gas flows. Phys Fluids 19:037102

Xu J, Zhao C (2007) Two-dimensional numerical simulations of shock waves in micro convergent–divergent nozzles. Int J Heat Mass Transf 50:2434–2438

Xue H, Ji HM, Shu C (2003) Prediction of flow and heat transfer characteristics in micro-Couette flow. Nanoscale Microscale Thermophys Eng 7:51–68

Yang J, Ye J, Zheng J, Wong I, Ma Y, Lam C, Link S (2009) Improving DSMC with new pressure boundary conditions for heat and mass transfer of microchannel flows. Nanoscale Microscale Thermophys Eng 13:165–183

Zhou Q, Leschziner MA (1999) An improved particle-locating algorithm for Eulerian–Lagrangian computations of two-phase flows in general coordinates. Int J Multiph Flow 25:813–825